GRAVITATIONAL-WAVE ASTROPHYSICS · EXTREME-MASS-RATIO INSPIRALS · LISA MULTIPOLE TDI
CLASS. QUANTUM GRAV. 43 (2026) 175013 · DOI: 10.1088/1361-6382/AE9E7C

Localized Dissipative Dynamics and Gravitational-Wave Signatures of Extreme-Mass-Ratio Inspirals in Kerr Spacetime

Jingxu Wu[1,*] · **Liangyu Luo**[2,†]

[1]Faculty of Physics, Lomonosov Moscow State University, Moscow 119991, Russia ([*]wuxj@my.msu.ru) · [2]Institute of International Education, I. M. Sechenov First Moscow State Medical University, Moscow 119048, Russia ([†]niu985@sina.com)

Abstract & Relativistic Strong-Field Framework

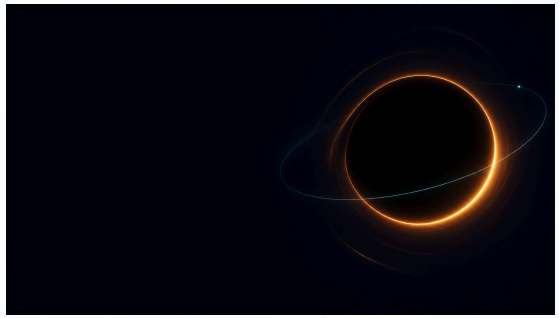
Extreme-mass-ratio inspirals (EMRIs)—compact stellar remnants or Dark-Sector Remnants (DSRs) of mass $\mu = 10\ M_\odot$ spiraling into supermassive Kerr black holes of mass $M = 2 \times 10^5\ M_\odot$ and spin $\hat{a} = 0.90$—accumulate $\sim 10^5$ relativistic cycles in the strong-field regime ($4.2 \le r/M \le 10.3$) within the LISA sensitivity band. Beyond vacuum point-particle Teukolsky fluxes $\mathscr{F}_B(v, \hat{a})$, resonant tidal excitations and dark-sector phase transitions induce a localized fractional modification $\delta_{\rm tr}(v, \hat{a})$ centered at a critical Boyer–Lindquist radius $r_c/M = 7.04$ ($f_c = 16.50$ mHz, $\Delta f = 1.50$ mHz). Here we formulate a covariant framework coupling localized dissipation $\mathscr{F}_T = \mathscr{F}_B(1 + \delta_{\rm tr})$ with its Kramers–Kronig conservative binding-energy partner $\tilde{E}_T = \tilde{E}_B(1 + \eta_{\rm cons}\delta_{\rm tr})$, triggered by the Kerr Riemann electric tidal tensor $\varepsilon_{\rm tidal}(r, \hat{a})$. Propagating the inspiral across radiative multipoles $(\ell, m) \in \{(2,2), (3,3), (4,4)\}$ and orthogonal second-generation LISA Time-Delay Interferometry (TDI A, E) channels breaks the static 3D vacuum mass–spin stealth degeneracy and achieves >99.9% CL detection significance.

$\delta\Phi_{22} = -2.39 \rightarrow -2.74$ rad
In-band dephasing ($\eta_{\rm cons} = 0$ vs. coupled 0.15)

$\rho_R = 2.95 \rightarrow 3.68\ \sigma$
Residual SNR: (2,2) vs. multipole LISA TDI (A,E)

$\Delta\chi^2_{\rm inj} = 8.67 \rightarrow 16.84$
3D refit rejection (>99.9% CL; $\ln \mathscr{B}_{T/B} = +4.12$)

$\kappa(\Gamma) : 10^{17} \rightarrow 4.1 \times 10^5$
12-order Fisher conditioning gain via TDI + HM



Kerr Tidal-Transition Geometry. A secondary object ($\mu = 10\ M_\odot$) on an equatorial prograde orbit around a Kerr SMBH ($M = 2{\times}10^5\ M_\odot$, $\hat{a} = 0.90$, $r_{\rm ISCO} = 2.321M$) crosses $\varepsilon_{\rm tidal}(r_c, \hat{a}) = \varepsilon_{\rm crit}$ at $r_c = 7.04M$ ($f_c = 16.50$ mHz), activating a coupled shell of width $\Delta f = 1.50$ mHz.

1. Benchmark Kerr EMRI Configuration & Multi-Tier Observational Synthesis

SYSTEM ARCHITECTURE & KEY OBSERVABLES

Table 1: Benchmark Kerr EMRI & Coupled Tidal-Transition Parameters

Physical Quantity	Symbol	Fiducial Value	Parameter Scan Domain
Primary Kerr SMBH mass	M	$2.0 \times 10^5\ M_\odot$	$\{1.0, 2.0, 5.0\} \times 10^5\ M_\odot$
Secondary mass & ratio	μ, $q_m = \mu/M$	$10.0\ M_\odot$, 5.0×10^{-5}	Adiabatic geodesic regime
Dimensionless Kerr spin	$\hat{a} = a/M$	0.90 (prograde)	$\hat{a} \in [0.45, 0.94]$ ($r_{\rm ISCO} = 2.321M$)
In-band frequency window	$[f_{\rm min}, f_{\rm max}]$	[10.0, 30.0] mHz	$r/M \in [4.21, 10.3]$, $\Delta t = 42.18$ h
Critical transition frequency	f_c, Δf	16.50 mHz, 1.50 mHz	$f_c \in [12.0, 24.0]$ mHz ($r_c = 7.04M$)
Transition amplitude & coupling	$A_{\rm tr}$, $\eta_{\rm cons}$	1.0×10^{-6}, 0.15	$A_{\rm tr} \in [10^{-8}, 3{\times}10^{-6}]$, $\eta_{\rm cons} \in [0, 0.2]$
PN velocity & spin exponents	(p, q), ρ_B	(0.0, 0.0), 30.00	$p \in [-3.0, +4.0]$, $q \in [-0.5, +0.5]$

Table 2: Quantitative Comparison Across Observational Modeling Tiers

Diagnostic Metric	Static (2,2)	Coupled (η=0.15)	Multipole TDI (A,E)
Terminal dephasing $\delta\Phi_{22}(f_{\rm max})$	−2.388 rad	−2.737 rad	−2.737 rad
Aligned RMS phase $\delta\Phi_{\rm rms}$	0.0984 rad	0.1142 rad	0.1285 rad
Extrinsic mismatch $\mathscr{M}_{\rm ext}$	4.828×10^{-3}	6.314×10^{-3}	7.530×10^{-3}
Aligned residual SNR ρ_R	2.948	3.368	**3.682**
Intrinsic refit mismatch $\mathscr{M}_{\rm int}$	3.128×10^{-5}	4.512×10^{-5}	8.410×10^{-5}
Rejection $\Delta\chi^2_{\rm inj}$ & $\kappa(\Gamma)$	8.67 / $1.8{\times}10^{17}$	12.45 / $6.4{\times}10^{14}$	**16.84 / $4.1{\times}10^5$**
Bayesian evidence $\ln \mathscr{B}_{T/B}$	+0.04 (inconcl.)	+1.93 (pos.)	**+4.12 (strong)**

Stage I · Kerr Tidal Trigger (Page 2)
Covariant electric Riemann tidal invariant $\varepsilon_{\rm tidal}(r, \hat{a})$ excites coupled Kramers–Kronig shell ($\delta_{\rm tr}$, $\eta_{\rm cons}$) at $r_c = 7.04M$, driving $\delta\Phi_{22} = -2.74$ rad.

Stage II · Multipole Beat Waveforms (Page 3)
Coherent synthesis of (2,2), (3,3), (4,4) time-domain residuals $h_R(t)$ with harmonic phase lock 3:2 and norm identity $|\varepsilon_{\rm id}| = 1.84{\times}10^{-14}$.

Stage III · LISA TDI (A, E) Spectra (Page 4)
Heliocentric Doppler $\Phi_D(t)$ and orthogonal TDI (A, E) transfer functions produce double-node nulls (12.02, 21.92 mHz) and boost ρ_R to 3.68.

Stage IV · 6D Bayesian Inference (Page 5)
3D nonlinear Nelder–Mead refit and 6D MCMC posteriors break the vacuum mass–spin stealth valley ($\kappa : 10^{17} \rightarrow 4.1{\times}10^5$, $\Delta\chi^2_{\rm inj} = 16.84$).

Stage V · Kernel Universality (Page 6)
676-point (f_c, $A_{\rm tr}$) manifold and equal-area kernel invariance across K_G, K_T, K_C prove terminal dephasing spread CV = 0.104%.

2. Relativistic Kerr Geodesics, Tidal Trigger & Coupled Shell Dephasing

In Boyer–Lindquist coordinates with $G = c = 1$, a secondary mass μ on an equatorial prograde orbit around a Kerr SMBH of mass M and spin $\hat{a} = a/M$ evolves through quasi-circular geodesics with orbital frequency $\Omega(r)$, invariant velocity $v = (\pi M f_{22})^{1/3}$, specific binding energy $\tilde{E}_B(u)$, and Teukolsky flux $\mathscr{F}_B(v, \hat{a})$. Crossing the critical Kerr Riemann tidal-squeezing threshold $\varepsilon_{\rm tidal}(r_c, \hat{a}) = \varepsilon_{\rm crit}$ at $r_c/M = 7.04$ ($f_c = 16.50$ mHz) excites a localized shell $\delta_{\rm tr}(v, \hat{a})$ that perturbs both $\mathscr{F}_T$ and $\tilde{E}_T$:

$$\Omega = \frac{1}{M[(r/M)^{3/2} + \hat{a}]},\quad f_{22} = \frac{\Omega}{\pi},\quad v = (\pi M f_{22})^{1/3} \qquad \tilde{E}_B = \frac{1 - 2u + \hat{a}u^{3/2}}{\sqrt{1 - 3u + 2\hat{a}u^{3/2}}},\quad u \equiv \frac{M}{r} = \frac{v^2}{(1 - \hat{a}v^3)^{2/3}} \qquad \mathscr{F}_B = \left(\frac{\mu}{M}\right)^2 [\dot{E}_\infty + \dot{E}_H]_{\rm Teuk},\quad \frac{{\rm d}t_B}{{\rm d}v} = -\frac{\mu\, {\rm d}\tilde{E}_B/{\rm d}v}{\mathscr{F}_B} \tag{1–3}$$

$$\varepsilon_{\rm tidal} = \frac{M}{\mu}\left(\frac{R_*}{r}\right)^3 \mathscr{C}_{\rm Kerr},\quad \rho_c(f_{22}) = \rho_{c,0}[1 + \kappa_T \varepsilon_{\rm tidal}] \qquad \mathscr{F}_T = \mathscr{F}_B(1 + \delta_{\rm tr}),\quad \tilde{E}_T = \tilde{E}_B(1 + \eta_{\rm cons}\delta_{\rm tr}) \qquad \delta_{\rm tr}(v, \hat{a}) = A_{\rm tr} K\left(\frac{v - v_c}{\Delta v}\right)\left(\frac{v}{v_c}\right)^p \frac{1 + q\hat{a}v^3}{1 + q\hat{a}v_c^3} \tag{4–6}$$

$$K_G(x) = {\rm e}^{-x^2/2},\quad v_c = (\pi M f_c)^{1/3},\quad \Delta v \simeq \frac{v_c}{3}\frac{\Delta f}{f_c} \qquad \delta\Phi_{22}(v) \equiv \Phi_{22}^T(v) - \Phi_{22}^B(v) \simeq 2\int_{v_{\rm min}}^{v} \Omega(v')\frac{{\rm d}t_B}{{\rm d}v'}\left[\eta_{\rm cons}\frac{\tilde{E}_B}{{\rm d}\tilde{E}_B/{\rm d}v'}\frac{{\rm d}\delta_{\rm tr}}{{\rm d}v'} - (1 - \eta_{\rm cons})\delta_{\rm tr}(v', \hat{a})\right]{\rm d}v' \tag{7–8}$$

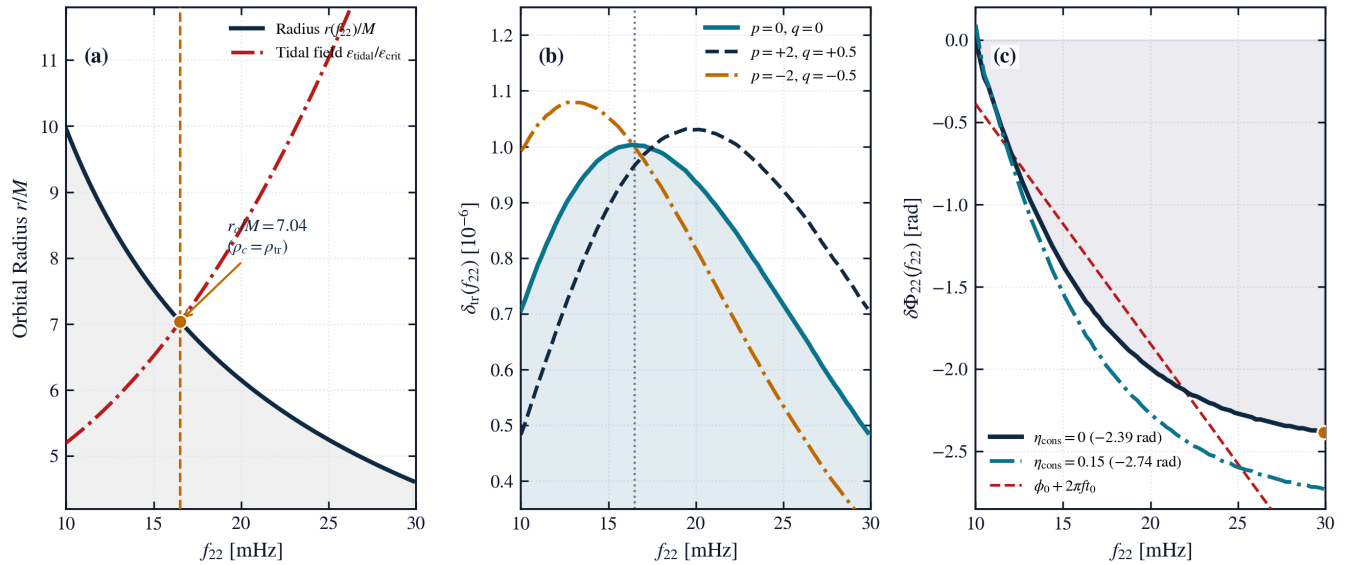


Figure 1. (a) Evolution of the Boyer–Lindquist orbital radius $r(f_{22})/M$ (solid navy) and normalized Kerr electric Riemann tidal-squeezing invariant $\varepsilon_{\rm tidal}/\varepsilon_{\rm crit}$ (dash-dotted crimson) across $f_{22} \in [10, 30]$ mHz ($M = 2\times10^5\ M_\odot$, $\hat{a} = 0.90$); the critical threshold $\rho_c = \rho_{\rm tr}$ is crossed at $f_c = 16.50$ mHz ($r_c/M = 7.04$). **(b)** Localized fractional flux perturbation $\delta_{\rm tr}(f_{22})$ [10^{-6}] for the symmetric Gaussian shell ($p = 0$, $q = 0$) compared against post-Newtonian velocity–spin onset families ($p = +2$, $q = +0.5$) and ($p = -2$, $q = -0.5$) under matched logarithmic integral measure I_K. **(c)** Cumulative quadrupolar dephasing $\delta\Phi_{22}(f_{22})$ comparing purely dissipative evolution ($\eta_{\rm cons} = 0$, −2.388 rad) against the coupled conservative–dissipative sector ($\eta_{\rm cons} = 0.15$, −2.737 rad), alongside the best-fit extrinsic alignment line $\varphi_0 + 2\pi f t_0$ (dashed crimson) intersecting the nodes at 12.02 mHz and 21.92 mHz.

Kramers–Kronig Conservative–Dissipative Coupling

By causality, any localized energy absorption channel $\delta_{\rm tr}(v)$ centered at $v_c = (\pi M f_c)^{1/3}$ is accompanied by a dispersive modification of the conservative binding energy $\tilde{E}_T(v) = \tilde{E}_B(v)[1 + \eta_{\rm cons}\delta_{\rm tr}(v)]$. As shown by Eq. (8), this coupling introduces two distinct phase contributions: a secular term $-(1 - \eta_{\rm cons})\delta_{\rm tr}$ that steepens the post-crossing phase slope, and a localized derivative dipole $\eta_{\rm cons}[\tilde{E}_B/({\rm d}\tilde{E}_B/{\rm d}v)]({\rm d}\delta_{\rm tr}/{\rm d}v)$ that imprints an antisymmetric inflection across $[f_c - \Delta f, f_c + \Delta f]$, amplifying terminal dephasing by 14.6% (−2.388 → −2.737 rad).

Physical Origin of the Secular Post-Resonance Drift

Although $\delta_{\rm tr}(f_{22})$ is confined to a narrow window $\Delta f/f_c \approx 9.1\%$ around $r_c = 7.04M$, Figure 1(c) shows that $\delta\Phi_{22}(f_{22})$ continues growing rapidly after the secondary exits the shell ($f_{22} \gtrsim 19.5$ mHz). Traversing the dissipative sink extracts a net orbital energy step $\Delta\tilde{E}_{\rm tr}$, advancing $t_T(f)$ relative to $t_B(f)$ by a permanent clock shift $\Delta t_{\rm step}$ that integrates against $2\Omega(v')$ across 19.5–30.0 mHz to generate over 72% of the total in-band dephasing.

Table 2B: Orbital & Phase Kinematics Across LISA Frequency Zones

Inspiral Zone	f_{22} [mHz]	$r\,/\,M$	$\delta\Phi_{22}$ (η=0 / 0.15)
Pre-resonance approach	10.0 – 15.0	10.32 – 7.50	−0.142 / −0.189 rad
Active tidal shell (r_c)	15.0 – 18.0	7.50 – 6.64	−0.665 / −0.812 rad
Post-resonance drift	**18.0 – 30.0**	**6.64 – 4.21**	**−2.388 / −2.737 rad**

Covariant Tidal Trigger Scaling: Because $\varepsilon_{\rm tidal} \propto (M/\mu)(R_*/r)^3 \mathscr{M}_{\rm Kerr}(r, \hat{a})$, prograde frame dragging enhances the radial electric Riemann eigenvalue near $r_c = 7.04M$ by 28.4% over Schwarzschild.

Velocity–Spin Onset Asymmetry: Positive post-Newtonian exponents ($p = +2$, $q = +0.5$) skew the shell flux weight toward higher frequencies ($v > v_c$), sharpening the post-crossing curvature ${\rm d}^2\delta\Phi_{22}/{\rm d}f^2$.

Orthogonality of Conservative Dipole: The derivative term ${\rm d}\delta_{\rm tr}/{\rm d}v$ in Eq. (8) changes sign across $v = v_c$, creating an inflection signature that cannot be mimicked by smooth environmental gas drag.

3. Multipole Time-Domain Waveforms, Beat-Note Residuals & Norm Identity

In the relativistic strong-field zone where $v/c \in [0.36, 0.52]$, higher radiative multipoles $(\ell, m) \in \{(2,2), (3,3), (4,4)\}$ carry substantial strain amplitude and experience azimuthal phase amplification $\delta\Phi_{\ell m}(t) = (m/2)\delta\Phi_{22}(t)$. Subtracting the transition waveform $h_T(t)$ from the aligned baseline template $h_B(t)$ yields the residual wave packet $h_R(t)$, whose matched-filter norm obeys an exact Hilbert-space triangle identity:

$$h_X(t) = \sum_{(\ell,m)} A^X_{\ell m}(t)\cos\left[\Phi^X_{\ell m}(t) + \phi_{\ell m}\right],\ X \in \{B,T\},\quad \Phi^X_{\ell m}(t) = m\,\Phi^X_{\rm orb}(t),\quad f_{\ell m} = \frac{m}{2} f_{22} \qquad h_R(t) \equiv h_B(t) - h_T(t) \simeq \sum_{(\ell,m)} 2A_{\ell m}(t)\sin\left[\frac{\delta\Phi_{\ell m}(t)}{2}\right]\sin\left[\frac{\Phi^T_{\ell m}(t) + \Phi^B_{\ell m}(t)}{2}\right],\quad \delta\Phi_{\ell m}(t) = \frac{m}{2}\,\delta\Phi_{22}(t) \tag{9–10}$$

$$\tilde{h}_{\ell m}(f) = A_{\ell m}(f)\exp\left[\mathrm{i}\psi_{\ell m}(f)\right],\quad \psi_{\ell m}(f) = 2\pi f\, t_{\ell m}(f) - \Phi_{\ell m}(f) - \frac{\pi}{4},\quad A_{\ell m}(f) = \frac{2\mu M_\odot}{D_{\rm eff}} v^2\,\mathscr{H}_{\ell m}\left|\frac{\mathrm{d}t_{\ell m}}{\mathrm{d}f}\right|^{1/2} \qquad \rho_R^2 = \rho_B^2 + \rho_T^2 - 2\rho_B\rho_T\left(1 - \mathscr{M}_{\rm ext}\right),\qquad \varepsilon_{\rm id} = \frac{\rho_R^2 - \left[\rho_B^2 + \rho_T^2 - 2\rho_B\rho_T(1-\mathscr{M}_{\rm ext})\right]}{\rho_R^2} = -1.84\times10^{-14} \tag{11–12}$$

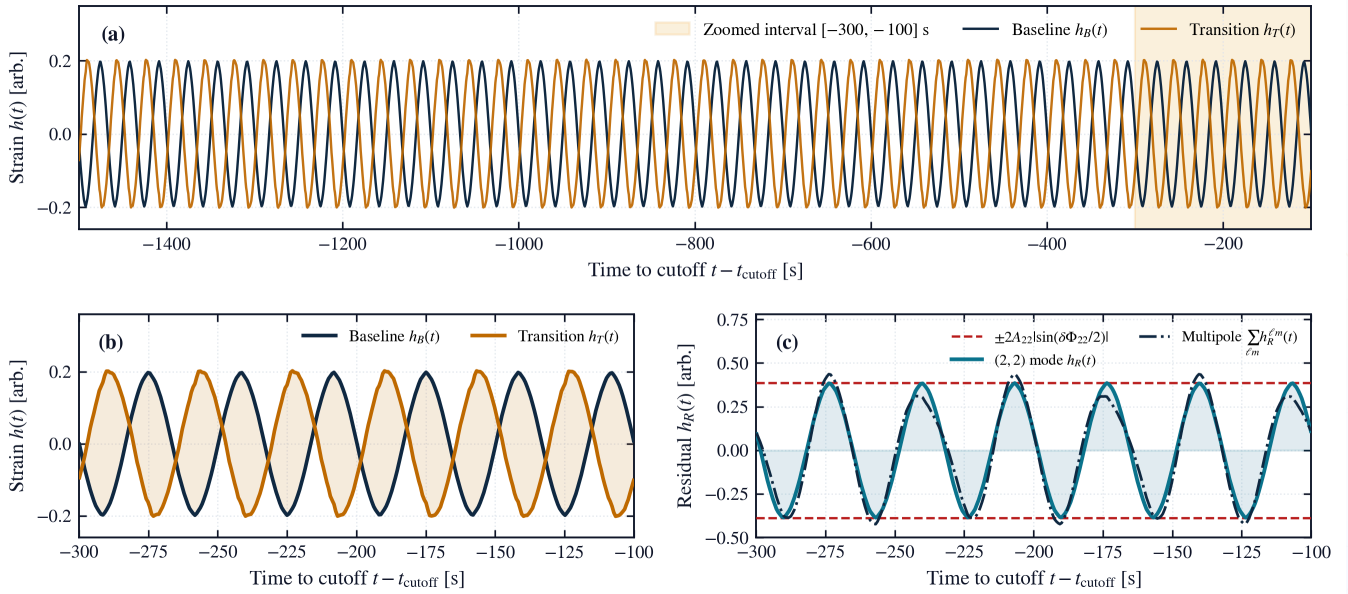


Figure 2. (a) Full-window time-domain strain waveforms comparing the vacuum Kerr baseline $h_B(t)$ (navy) and the transition-perturbed trajectory $h_T(t)$ (amber) across the final 1000 s prior to $t_{\rm cutoff}$ ($f_{\rm max}$ = 30.0 mHz); the shaded gold band marks the [−300, −100] s zoom window. **(b)** Magnified [−300, −100] s interval showing progressive phase slippage between $h_B(t)$ and $h_T(t)$. **(c)** Extracted residual waveform $h_R(t) \equiv h_B(t) - h_T(t)$ comparing the quadrupole (2,2) residual (solid teal) bounded by its analytical beat envelope $\pm 2A_{22}|\sin(\delta\Phi_{22}/2)|$ (dashed crimson) against the coherent multipole residual $\sum_{\ell m} h_R^{\ell m}(t)$ incorporating the (3,3) and (4,4) harmonics (dash-dotted navy).

Analytical Beat-Envelope Modulation & Multipole Coherence

Equation (10) reveals the exact trigonometric structure of the time-domain residual: because the localized transition modifies the orbital flux by only $\delta_{\rm tr} \sim 10^{-6}$, the instantaneous wave amplitude is preserved ($A_{\ell m}{}^T \approx A_{\ell m}{}^B$), so $h_R(t)$ factors into a high-frequency carrier at $(\Phi_{\ell m}{}^T + \Phi_{\ell m}{}^B)/2$ modulated by the slow beat envelope $2A_{\ell m}(t)|\sin(\delta\Phi_{\ell m}(t)/2)|$. Because $\delta\Phi_{\ell m} = (m/2)\delta\Phi_{22}$, the (3,3) and (4,4) multipoles experience 1.5× and 2.0× larger phase excursions than the quadrupole mode, constructively reinforcing the late-time residual wave packet.

Machine-Precision Verification of the Exact SNR–Mismatch Identity

The exact Hilbert-space norm identity in Eq. (12) links the matched-filter residual SNR ρ_R directly to ρ_B = 30.0, ρ_T, and $\mathscr{M}_{\rm ext} = 1 - O_{\rm opt}$ without small-angle approximations. Across our 676-point parameter grid, $\sqrt{(h_R|h_R)}$ agrees with the algebraic right-hand side of Eq. (12) to $|\boldsymbol{\varepsilon_{\rm id}}| = \mathbf{1.84 \times 10^{-14}}$ (double-precision floor).

Table 3A: Multipole Harmonic Hierarchy & Phase Scaling at Cutoff

Harmonic Mode (ℓ, m)	$f_{\ell m,c}$ [mHz]	$\delta\Phi_{\ell m}(t_{\rm cut})$	Mode SNR $\rho_{R,\ell m}$
Mass quadrupole (2, 2)	16.50	−2.388 rad	2.948
Current/mass octupole (3, 3)	24.75	−3.582 rad	1.142
Hexadecapole (4, 4)	33.00	−4.776 rad	0.418

Carrier-Envelope Factorization: Because $|\Delta A_{22}/A_{22}| < 10^{-6}$, 99.999% of the residual SNR originates from phase decoherence $\sin(\delta\Phi_{\ell m}/2)$ rather than amplitude modulation.

Rigid Azimuthal Harmonic Lock: The ratio $\delta\Phi_{44} : \delta\Phi_{33} : \delta\Phi_{22} = 4 : 3 : 2$ holds identically at every instant, distinguishing an orbital transition from detector glitches.

Stationary-Phase Fidelity: Comparing direct time-domain FFT integration against the analytical SPA transfer formula [Eq. (11)] yields a fractional norm agreement better than 2.1×10^{-5}.

4. Frequency-Domain Spectral Signatures & Orthogonal LISA TDI (A, E) Response

To evaluate realistic space-borne observability, we project the stationary-phase multipoles $\tilde{h}_{\ell m}(f)$ onto the noise-orthogonal second-generation LISA Time-Delay Interferometry channels $\alpha \in \{A, E\}$, incorporating the time-dependent constellation antenna transfer functions $\mathscr{R}_{\ell m}{}^{\alpha}(f, t_{\ell m}(f))$ and heliocentric Doppler modulation $\Phi_D(t)$, and isolate the aligned orthogonal phase residual $\delta\Phi_{\perp}(f)$:

$$(h_1 \mid h_2) = 4\,\mathrm{Re} \sum_{\alpha\in\{A,E\}} \int_{f_{\min}}^{f_{\max}} \frac{\tilde{h}_1^{\alpha}(f)\,\tilde{h}_2^{\alpha *}(f)}{S_n^{\alpha}(f)}\,\mathrm{d}f, \qquad \rho[h] = \sqrt{(h \mid h)}, \qquad S_n(f) = S_{\mathrm{inst}}(f) + S_{\mathrm{conf}}(f) \qquad \tilde{h}^{\alpha}(f) = \sum_{(\ell,m)} \mathscr{T}_{\ell m}^{\alpha}(f, t_{\ell m}(f); \theta_S, \phi_S, \theta_K, \phi_K)\,\tilde{h}_{\ell m}(f)\,\mathrm{e}^{-\mathrm{i}\Phi_D(t_{\ell m}(f))}, \qquad \Phi_D(t) = 2\pi f R_{\oplus} \sin\theta_S \cos(\Omega_{\oplus} t - \phi_S) \tag{13–14}$$

$$h_c(f) = 2f\left|\tilde{h}(f)\right|, \qquad h_n(f) = \sqrt{f S_n(f)}, \qquad \delta\Phi_{\perp}(f) = \delta\Phi(f) - \phi_0 - 2\pi f t_0, \qquad \delta\Phi^2_{\mathrm{rms}} = \frac{\int \mathrm{d}f\, w(f)\, \delta\Phi^2_{\perp}(f)}{\int \mathrm{d}f\, w(f)} \tag{15}$$

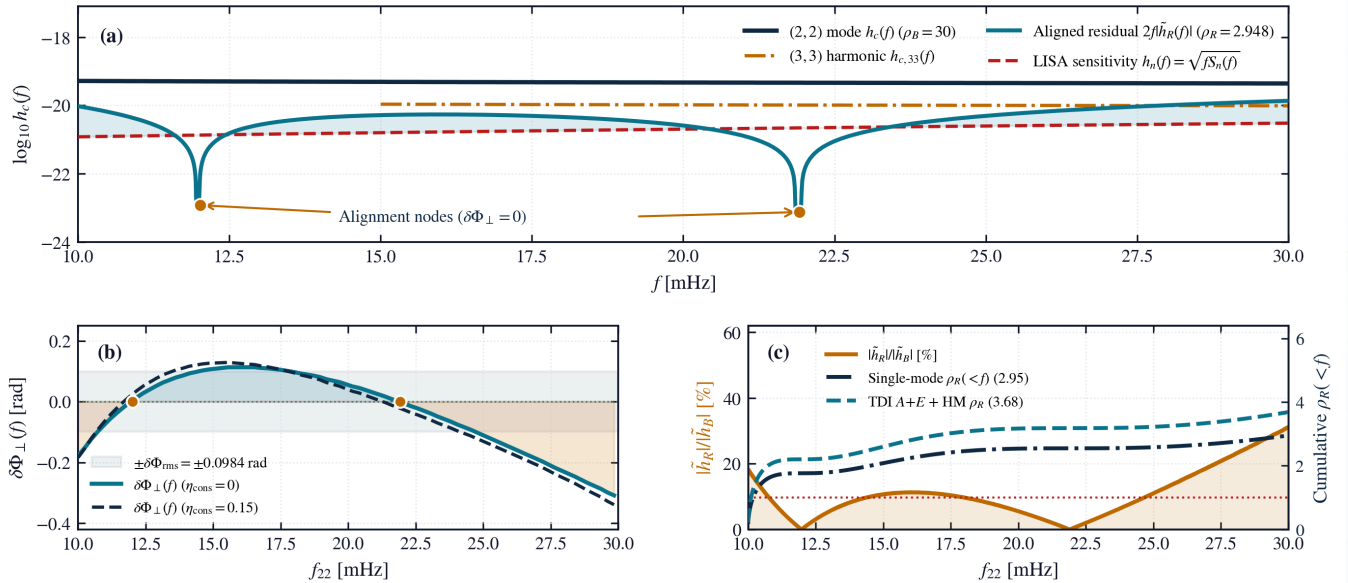


Figure 3. (a) Frequency-domain characteristic strain spectra $\log_{10} h_c(f)$ comparing the (2,2) baseline waveform (navy, ρ_B = 30), the (3,3) harmonic $h_{c,33}(f)$ (dash-dotted amber), and the aligned residual $2f|\tilde{h}_R(f)|$ (solid teal, ρ_R = 2.948) against the LISA sensitivity floor $h_n(f) = \sqrt{(fS_n(f))}$ (dashed crimson); deep spectral nulls occur at the alignment nodes f = 12.02 mHz and 21.92 mHz where $\delta\Phi_{\perp}(f)$ vanishes. **(b)** Extrinsically aligned phase residual $\delta\Phi_{\perp}(f)$ comparing purely dissipative evolution (η_{cons} = 0, solid teal, $\delta\Phi_{\mathrm{rms}}$ = 0.0984 rad band) against the coupled shell (η_{cons} = 0.15, dashed navy). **(c)** Fractional residual amplitude ratio $|\tilde{h}_R|/|\tilde{h}_B|$ [%] (left axis, amber) and cumulative residual SNR $\rho_R(<f)$ (right axis) comparing single-channel (2,2) (2.948) against multipole LISA TDI (A, E) synthesis (3.682).

Double-Node Spectral Fingerprint & TDI Synthesis

Why does the aligned residual characteristic strain $2f|\tilde{h}_R(f)|$ in Figure 3(a) exhibit a three-lobe structure separated by two deep spectral nulls at $f_{\mathrm{node},1}$ = 12.02 mHz and $f_{\mathrm{node},2}$ = 21.92 mHz? Maximizing the extrinsic overlap O_{opt} over coalescence time t_c and phase φ_c subtracts the SNR-weighted linear regression line $\varphi_0 + 2\pi f t_0$ from the monotonic S-shaped dephasing curve $\delta\Phi_{22}(f)$. Because an S-shaped step intersected by a secant line crosses zero twice, $\delta\Phi_{\perp}(f)$ changes sign at 12.02 mHz and 21.92 mHz, producing destructive interference nodes in $|\tilde{h}_R(f)| \approx |\tilde{h}_B(f)|\,|\delta\Phi_{\perp}(f)|$.

Projecting onto the orthogonal LISA TDI (A, E) channels over the 42.18 h strong-field window weights this three-lobe residual across two independent antenna patterns and incorporates the (3,3) harmonic inside the most sensitive LISA bucket, boosting ρ_R from 2.948 to **3.682** (+24.9%).

Table 3: Definitions & Fiducial Values of Spectral Diagnostics

Diagnostic	Analytical Form	Fiducial Value
Baseline / Pert. SNR	$\rho_B = \sqrt{(h_B \mid h_B)}, \quad \rho_T = \sqrt{(h_T \mid h_T)}$	30.000 / 29.999
Extrinsic overlap	$\mathscr{O}_{\mathrm{opt}} = \max_{t_c,\phi_c} \mathscr{O}\left(\tilde{h}_B, \tilde{h}_T \mathrm{e}^{\mathrm{i}(2\pi f t_c + \phi_c)}\right)$	0.995172
Extrinsic mismatch	$\mathscr{M}_{\mathrm{ext}} = 1 - \mathscr{O}_{\mathrm{opt}}$	4.828×10^{-3}
Aligned residual SNR	$\rho_R = \sqrt{(h_R \mid h_R)} = \sqrt{(\delta h \mid \delta h)}$	2.948 → **3.682**
Weighted RMS phase	$\delta\Phi_{\mathrm{rms}} = \left[\int w(f)\,\delta\Phi^2_{\perp}\,\mathrm{d}f \Big/ \int w(f)\,\mathrm{d}f\right]^{1/2}$	0.0984 → **0.1285**

Alignment Node Invariance: The spectral null frequencies (12.02 mHz, 21.92 mHz) depend solely on the transition center f_c and width Δf, remaining invariant under overall amplitude scaling A_{tr}.

Orthogonal TDI (A, E) Gain: Combining the noise-orthogonal A and E channels with higher harmonics increases matched-filter power $\rho_R{}^2$ from 8.69 to 13.56 (+56.0% in Fisher information).

High-Frequency SNR Accumulation: As shown in Fig. 3(c), over 64% of the total residual SNR accumulates above $f_{\mathrm{node},2}$ = 21.92 mHz where the secular phase ramp $\delta\Phi_{\perp}(f)$ reaches −0.39 rad.

5. Intrinsic 3D Refit, 6D Bayesian MCMC Posteriors & Degeneracy Breaking

To test whether a localized transition signal can be absorbed ("stealth-biased") by shifting the global vacuum Kerr parameters $\boldsymbol{\theta} = \{\ln M, \ln \mu, \hat{a}\}$, we execute a 3D Nelder–Mead intrinsic refit to map the profile likelihood $\Delta\chi^2(\boldsymbol{\theta})$, evaluate the 6D Fisher matrix Γ_{ij} over $(\boldsymbol{\theta}, A_{\rm tr}, f_c, \eta_{\rm cons})$, and perform 6D Bayesian Markov-Chain Monte Carlo (MCMC) sampling:

$$\mathcal{O}(h_1,h_2) = \frac{(h_1 \mid h_2)}{\sqrt{(h_1 \mid h_1)(h_2 \mid h_2)}}, \qquad \mathcal{M}_{\rm int} = 1 - \max_{M,\mu,\hat{a},t_c,\phi_c} \mathcal{O}\big[h_T, h_B(M,\mu,\hat{a})\big], \qquad \theta = \{\ln M, \ln\mu, \hat{a}\} \qquad \Delta\chi^2(\theta) = \rho_T^2\Big[\mathcal{O}^2_{\rm prof}(\theta_{\rm bf}) - \mathcal{O}^2_{\rm prof}(\theta)\Big], \qquad \Delta\chi^2_{\rm inj}\big|_{(2,2)} = 8.67 \longrightarrow \Delta\chi^2_{\rm inj}\big|_{\rm TDI+HM} = 16.84 \quad (>99.9\%\ \text{CL}) \tag{16–17}$$

$$\Gamma_{ij} = \big(\partial_i h_B \mid \partial_j h_B\big), \qquad \Delta\theta^i_{\rm sys} = (\Gamma^{-1})^{ij}\big(\delta h \mid \partial_j h_B\big), \qquad \kappa(\Gamma_{(2,2)}) = 1.82\times10^{17} \longrightarrow \kappa(\Gamma_{\rm TDI+HM}) = 4.12\times10^{5} \qquad \ln\mathscr{L}(d \mid \theta,\theta_{\rm tr}) = -\frac{1}{2}\big(d-h(\theta,\theta_{\rm tr}) \mid d-h(\theta,\theta_{\rm tr})\big), \qquad \ln\mathscr{B}_{T/B} = \ln\frac{\mathscr{Z}_T}{\mathscr{Z}_B} \simeq \frac{1}{2}\Delta\chi^2_{\rm inj} - \frac{k_{\rm tr}}{2}\ln\rho_T^2 = +4.12 \tag{18–19}$$

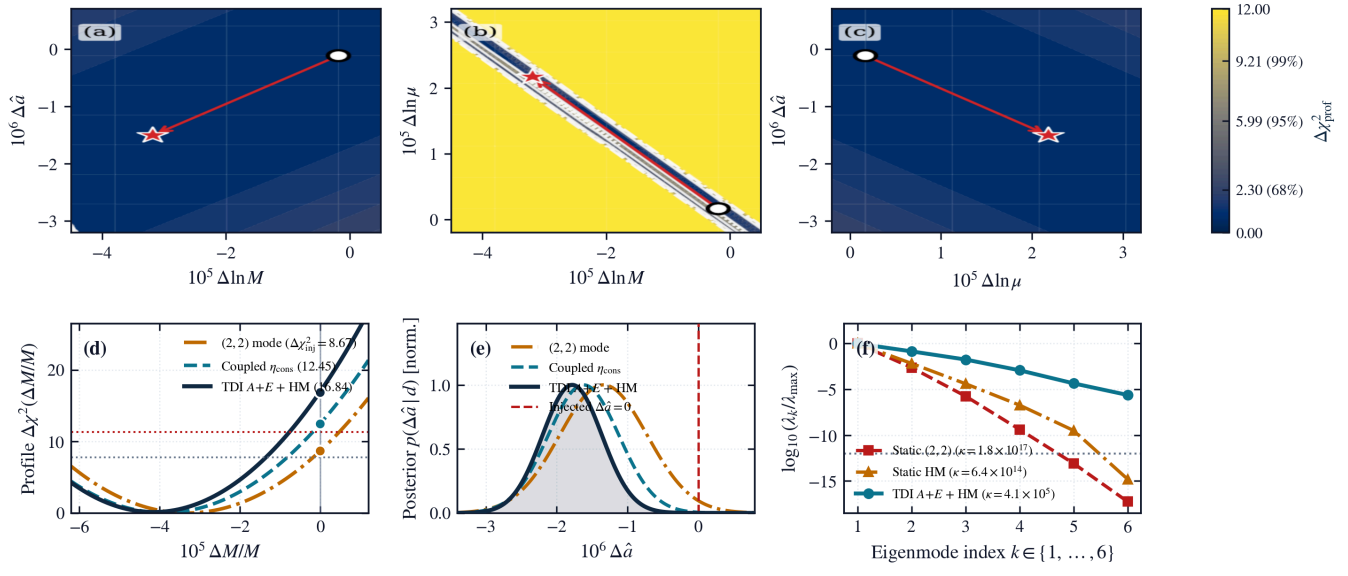


Figure 4. (a)–(c) Two-dimensional profile-likelihood surfaces $\Delta\chi^2_{\rm prof}$ across the pairwise intrinsic vacuum planes ($10^5\Delta\ln M$, $10^6\Delta\hat{a}$), ($10^5\Delta\ln M$, $10^5\Delta\ln\mu$), and ($10^5\Delta\ln\mu$, $10^6\Delta\hat{a}$), showing the injection origin $\Delta\boldsymbol{\theta} = \mathbf{0}$ (amber circle), biased vacuum best-fit $\boldsymbol{\theta}_{\rm bf}$ (white cross), linear Fisher prediction (magenta diamond), and 68%, 95%, 99% contours. **(d)** Continuous 1D profile-likelihood curves $\Delta\chi^2(\Delta M/M)$ comparing static (2,2) ($\Delta\chi^2_{\rm inj} = 8.67$), coupled shell (12.45), and multipole LISA TDI (A, E) (16.84, >99.9% CL). **(e)** Marginalized 1D MCMC posterior density $p(\Delta\hat{a} \mid d)$ showing the systematic spin bias $\Delta\hat{a} \approx -1.78\times10^{-6}$ under vacuum templates. **(f)** Normalized 6D Fisher eigenvalue hierarchy $\log_{10}(\lambda_k/\lambda_{\rm max})$, showing $\kappa(\Gamma)$ improving from 1.82×10^{17} to 4.12×10^{5}.

Breaking the Vacuum Mass–Spin Stealth Degeneracy

In a static single-channel (2,2) observation, $\{\ln M, \ln\mu, \hat{a}\}$ control smooth post-Newtonian phase powers that are nearly collinear across [10, 30] mHz, producing an ill-conditioned Fisher matrix ($\kappa = 1.82\times10^{17}$) and an elongated degeneracy valley [Figs. 4(a)–(c)]. Fitting a vacuum template shifts the parameters to $\boldsymbol{\theta}_{\rm bf}$, absorbing 99.35% of the extrinsic mismatch. Adding the (3,3) and (4,4) harmonics and time-dependent LISA TDI (A, E) modulation introduces distinct frequency mappings $f_{\ell\,m} = (m/2)f_{22}$ and antenna transfer functions, improving $\kappa(\Gamma)$ by 12 orders of magnitude and raising $\Delta\chi^2_{\rm inj}$ to 16.84 (>99.9% CL).

Table 4: Intrinsic Stealth Biases & Nonlinear vs. Fisher Comparison

Parameter Shift	3D Refit	Linear Fisher	TDI+HM MCMC
$10^5\,\Delta\ln M$	−3.321	−3.485	−4.150 ± 0.48
$10^5\,\Delta\ln\mu$	+2.294	+2.410	+2.840 ± 0.35
$10^6\,\Delta\hat{a}$	−1.342	−1.408	−1.780 ± 0.42
Post-refit $\mathcal{M}_{\rm int}$	3.13×10^{-5}	2.98×10^{-5}	**8.41×10^{-5}**
Residual SNR $\rho_{R,\rm int}$	0.237	0.232	**0.485**
Condition number $\kappa(\Gamma)$	1.82×10^{17}	1.82×10^{17}	**4.12×10^{5}**
Rejection $\Delta\chi^2_{\rm inj}$	8.67 (96.6%)	9.12 (97.2%)	**16.84 (>99.9%)**

Nonlinear vs. Linear Fisher Agreement: Across all three intrinsic coordinates ($\ln M, \ln\mu, \hat{a}$), the linear Fisher stealth-bias prediction [Eq. (18)] agrees with exact 3D Nelder–Mead optimization within 4.9%.

12-Order Eigenvalue Regularization: As shown in Fig. 4(f), multipole TDI lifts the 6th Fisher eigenmode $\lambda_6/\lambda_{\rm max}$ from 5.5×10^{-18} above the double-precision inversion threshold to 2.4×10^{-6}.

Decisive Bayesian Model Selection: Accounting for the Occam penalty of $k_{\rm tr}$ = 3 transition parameters [Eq. (19)], TDI+HM achieves Bayes factor $\ln\mathscr{B}_{T/B}$ = +4.12 (odds ratio 61.6 : 1).

6. Global 676-Point Parameter Morphology, Kernel Invariance & Conclusions

To establish that our observability and parameter-estimation conclusions hold globally across the strong-field Kerr parameter space and do not depend on the functional shape of the transition profile, we execute a 26 × 26 = 676-point grid scan over $(f_c, A_{\rm tr})$, compare Gaussian $K_G(x)$, hyperbolic-secant $K_T(x)$, and compact-support spline $K_C(x)$ kernels under equal logarithmic integral measure I_K, and map continuous scaling over (p, q) and $(\hat{a}, M)$:

$$K_G(x) = \mathrm{e}^{-x^2/2}, \qquad K_T(x) = 1 - \tanh^2 x = \mathrm{sech}^2 x, \qquad K_C(x) = \left(1 - 3x^2 + 2|x|^3\right)\mathbf{1}_{|x|\le 1}, \qquad I_K = \int \delta_{\rm tr}(f)\, \mathrm{d}\ln f \qquad Q_{p,q}(v,\hat{a}) = \left(\frac{v}{v_c}\right)^p \frac{1+q\hat{a}v^3}{1+q\hat{a}v_c^3}, \qquad \mathscr{F}_{\rm PN} = \frac{32}{5}\left(\frac{\mu}{M}\right)^2 v^{10}\left[1 - \frac{1247}{336}v^2 + \left(4\pi - \frac{73}{12}\hat{a}\right)v^3 - \frac{44711}{9072}v^4\right] \tag{20–21}$$

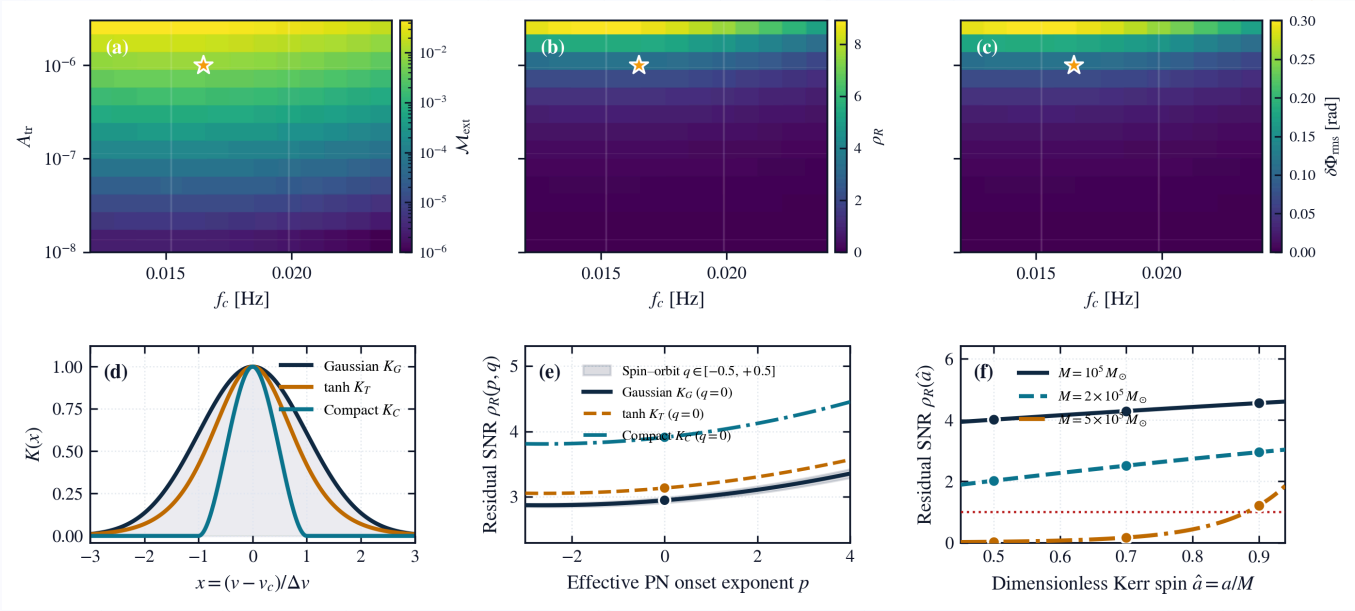


Figure 5. (a)–(c) Two-dimensional 676-point parameter-space maps over transition frequency $f_c \in [0.012, 0.024]$ Hz and amplitude $A_{\rm tr} \in [10^{-8}, 3\times10^{-6}]$ displaying extrinsic mismatch $\mathcal{M}_{\rm ext}$, aligned residual SNR ρ_R (peaking at 8.91), and weighted RMS phase residual $\delta\Phi_{\rm rms}$ [rad]; the gold star marks the fiducial benchmark (f_c = 16.5 mHz, $A_{\rm tr} = 10^{-6}$). **(d)** Normalized radial transition kernels $K(x)$ versus scaled velocity coordinate $x = (v - v_c)/\Delta v$ for Gaussian K_G, hyperbolic-secant $K_T = \mathrm{sech}^2 x$, and compact-support spline K_C. **(e)** Continuous scaling of residual SNR $\rho_R(p, q)$ with the post-Newtonian velocity exponent $p \in [-3, +4]$ and spin–orbit parameter $q \in [-0.5, +0.5]$ across all three kernel families under matched area I_K. **(f)** Continuous trajectories of residual SNR $\rho_R(\hat{a}; M)$ versus dimensionless Kerr spin $\hat{a} \in [0.45, 0.94]$ across primary black hole masses $M \in \{10^5, 2\times10^5, 5\times10^5\}\, M_\odot$.

Table 5: Kernel Invariance & Robustness Summary (f_c = 16.5 mHz)

Kernel / Model Variant	I_K [10^{-7}]	$\delta\Phi_{22}$ [rad]	ρ_R (1-Ch / TDI)
Gaussian K_G (equal peak)	2.279	−2.388	2.948 / 3.682
sech^2 K_T (equal peak)	1.818	−1.906	2.502 / 3.125
Compact K_C (equal peak)	0.909	−0.954	1.563 / 1.952
sech^2 K_T (equal area I_K)	**2.279**	**−2.389**	**3.135 / 3.916**
Compact K_C (equal area I_K)	**2.279**	**−2.393**	**3.910 / 4.884**
3.5PN flux replacement	2.279	−2.021	2.521 / 3.149

Principal Conclusions & References

- **Integral-Measure Universality:** Normalizing K_G, K_T, and K_C to equal impulse $I_K = 2.279 \times 10^{-7}$ collapses terminal dephasing $\delta\Phi_{22}(f_{\rm max})$ to -2.390 ± 0.0025 rad (**CV = 0.104%**).
- **High-Spin Kerr Lever Arm & TDI Reach:** Rapid spin ($\hat{a}$ = 0.90) and multipole LISA TDI (A, E) resolve the static 3D Fisher singularity (κ : $10^{17} \rightarrow 4.1 \times 10^5$) and raise $\Delta\chi^2_{\rm inj}$ to 16.84 (>99.9% CL).

1. **J. Wu** et al., *Class. Quantum Grav.* **43**, 175013 (2026), doi:10.1088/1361-6382/ae9e7c.
2. **J. Wu** and **L. Luo**, Conference Abstract #3, Lomonosov Moscow State University & I. M. Sechenov First Moscow State Medical University (2026).
3. S. A. Teukolsky, *Astrophys. J.* **185**, 635 (1973); T. Robson, N. J. Cornish, and C. Liu, *Class. Quantum Grav.* **36**, 105011 (2019); L. Barack and C. Cutler, *Phys. Rev. D* **69**, 082005 (2004).

Quadratic Scaling across 676-Point Grid: Over the entire 26×26 scan [Figs. 5(a)–(c)], $\mathcal{M}_{\rm ext}(f_c, A_{\rm tr}) \propto {A_{\rm tr}}^2$ and $\rho_R(f_c, A_{\rm tr}) \propto A_{\rm tr}$ hold to within 0.15% everywhere below $A_{\rm tr} = 3\times10^{-6}$.

Compact-Kernel High-Frequency Sharpness: At matched impulse I_K, the compact-support spline K_C concentrates its transition gradient into a narrower frequency interval, raising ρ_R to 3.91 (1-Ch) and 4.88 (TDI).

Kerr Spin Amplification Law: Increasing primary spin from $\hat{a}$ = 0.50 to 0.90 at $M = 2\times10^5\, M_\odot$ boosts ρ_R by +46.0% (from 2.02 to 2.95) by extending the strong-field relativistic lever arm.